Special Feature: GaN for Opto- and Power-electronic Applications (2)

Characterization of GaN-related materials using high-resolution XRD

Katsuhiko Inaba*

1. Introduction

Although high-resolution X-ray diffraction (HR-XRD) has been commonly employed for the crystallinity characterization of GaN-related materials, special care is required due to the complexities resulting from peculiar features in GaN-related materials, as explained in the preceding article.

General explanation for the application of HR-XRD techniques to the characterization of semiconductor epitaxial films or bulk single crystals can be found in various textbooks[(1)–(5)]. Therefore, this article will focus on special considerations to be taken in the application of the HR-XRD technique to GaN and related opto-electronic and power-electronic device materials. In addition, the latest hot topics in the HR-XRD characterization techniques for GaN-related materials will be shortly reviewed.

2. Crystallographic features of GaN

Let us start with the crystal structure of GaN.

The stable crystal structure of GaN at ambient conditions is the hexagonal wurtzite (WZ) type structure (Fig. 1) with the space group notation of $P6_3mc$. ZnO (zinc oxide), which has been widely studied for the application of light-emitting diodes or the transparent conductive oxide electrodes, is also stable with the WZ type structure in ambient conditions.

A metastable form of GaN with the cubic zincblende (ZB) type structure, which is the same crytsallographic structure of GaAs (gallium arsenide), has also been reported[(6)]. Under extreme conditions at high temperature and high pressure, ZnO and GaN are reported (or theoretically expected) to transform to the rocksalt (RS) type structure[(7)]. This transformation from the tetrahedrally coordinated WZ form to the octahedrally coordinated RS form leads to densification.

The crystal structure of WZ type GaN is shown in Fig. 1. The frame with black lines in the figure shows the unit cell of this crystal structure. Gallium atoms and nitrogen atoms each form a hexagonal closest packing (hcp) lattice. Each hcp lattice is shifted by the length of *uc* along *c*-axis. (*c* is the length of *c*-axis, and *u* is the fractional coordination along the *c*-axis. See more details on the next page.)

A Ga atom is coordinated with four nitrogen atoms, and a nitrogen atom is coordinated with four Ga atoms.

The blue narrow lines in Fig. 1 show one of the four-fold coordinated tetrahedrons of the Ga-N4, and the red thick lines show four Ga-N bonds in the Ga-N4 tetrahedron.

One of four Ga-N bonds, which is running vertically, thus, parallel to *c*-axis of the WZ unit cell, was shown as a line with an arrow in its end. This arrow shows the direction from a Ga atom to a nitrogen atom. This direction is defined as the + (positive) direction of *c*-axis.

In the case of WZ type GaN, the *c*-axis is the unique axis defining the crystallographic polarity. The direction

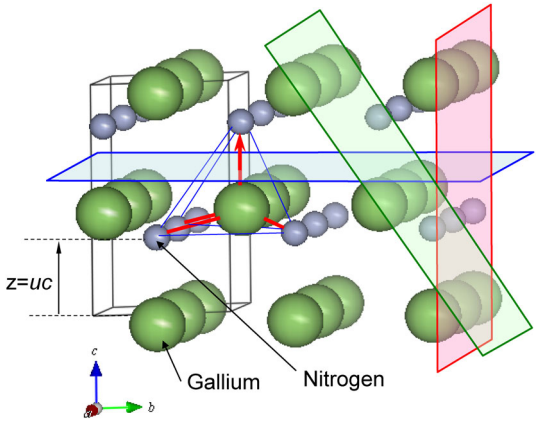

Fig. 1. Atomic arrangement in crystal structure of GaN with a wurtzite type structure.

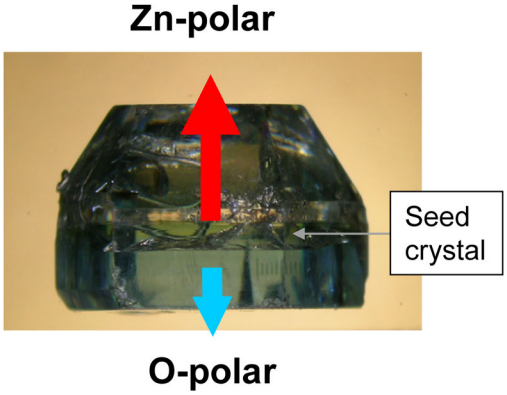

Fig. 2. A photograph of ZnO single crystal grown by the hydrothermal method.

* X-ray Research Laboratory, Rigaku Corporation.

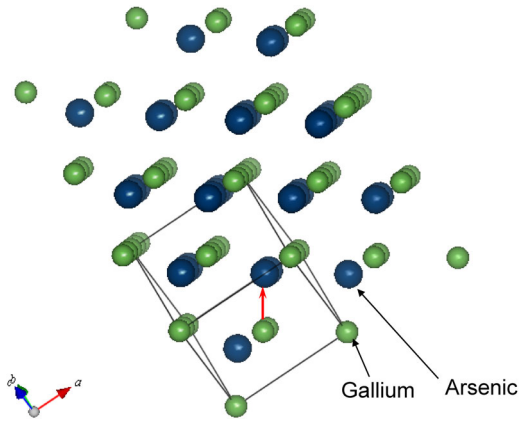

Fig. 3. Atomic arrangements of a zincblende type crystal structure.

from a Ga atom to a nitrogen atom along the *c*-axis of WZ lattice is defined as + (positive or plus) direction ([0001] or Ga-polar direction) and the direction from a nitrogen atom to a Ga atom along the *c*-axis is defined as − (negative or minus) direction ([000$\bar{1}$] or N-polar direction).

The polarity definition and the method to determine the polarity is reported by Hellmann in a precise review[8].

Three major lattice planes are shown in Fig. 1. A blue frame is (0001), a red frame is (1$\bar{1}$00), and a green frame is (1$\bar{1}$01).

The photograph of the ZnO single crystal which is the same crystal structure as GaN is shown in Fig. 2. The facetting planes of this crystal show a good correspondence with the lattice planes shown in Fig. 1. As reference, the crystal structure of GaAs with a ZB form is shown in Fig. 3. Atomically closed packing lattice planes ((0001) for the WZ type structure and (111) for a ZB type structure) were arranged to align horizontally. The crystallographic polar direction in the WZ type structure is <111> (a family of [111] directions).

In Fig. 1, all the vertical bonds from Ga atoms to nitrogen atoms along *c*-axis were directed as upward (the red arrow with the bold line in Fig. 1).

When a nitrogen atom is in the position where *u* of *uc* is 3/8 (=0.375), a Ga atom is located in the center of gravity of the four-fold coordinated Ga-N4 tetrahedron, electrostatic charges of all atoms are balanced and the spontaneous (intrinsic) polarization is neutralized. However, this balance will be broken and the spontaneous polarization will be produced when the *u* value (this value is crystallographically called the "*u*-parameter") deviates from 3/8 (=0.375).

The values for *u*-parameters for GaN is reported as 0.376[9] and for ZnO, *u*=0.3817 to 0.3856[10]–[12]. (See also the Table 1 in the preceding article.)

Since the band structure in the heteroepitaxial interfaces will be affected by the spontaneous polarization, there have been recent attempts to control the crystallographic polarity of epitaxially grown films[13].

Elastic deformations in pseudomorphic epitaxial films will promote the piezoelectric polarization, and as a result, this piezoelectric polarization will be added to the spontaneous polarization.

It should be noted here that the crystallographic polarity is defined by the three dimensional atomic arrangements, thus by the bulk physical properties of atomic arrangement. This bulk nature of a single crystal will determine the atoms to terminate the single crystal surface. In the case of a GaN single crystal, Ga atoms will terminate for a Ga-polar face and nitrogen atoms will terminate for a N-polar face (see also Fig. 1). The surface termination will be modified after exposure to air, partially because of the atomic migrations and partially of absorption of gaseous phases.

3. Characterization of GaN epitaxial films using HR-XRD

In this chapter, some topics concerning the characterization of GaN-related epitaxial films using HR-XRD will be described.

3.1. The importance of sample alignment and axis alignment

Since a GaN thin film is generally grown as a single crystalline epitaxial thin film on certain substrates with various thicknesses, the surface of GaN thin film samples must be aligned to the center of the HR-XRD goniometer. In addition, the axis alignment procedure for satisfying the diffraction condition for the reflections of interest is required.

The procedure to align the sample surface to the center of the goniometer (called the "direct beam half cut alignment") can be done with the direct beam position of the incident X-rays.

$2\theta/\omega$ profiles of the *c*-axis grown GaN thin film sample, 2μm in thickness on (0001) of sapphire (Sap) substrates are shown in Fig. 4(a). The GaN 0002 reflections and Sap 0006 reflections can be seen.

Close-up views around the GaN 0002 reflections and the Sap 0006 reflections are shown in Fig. 4(b) and Fig. 4(c), respectively.

Five profiles were shown in Fig. 4.

Red: without any sample alignment.

Blue: only with the alignment for sample thickness.

Sax Blue: with the axis alignment for Sap 0006 after **Blue**.

Pink: with the axis alignment for GaN 0002 after **Blue**.

Green: the sample was rotated by 10° with ϕ axis, and with the axis alignment for GaN 0002 after **Sax Blue**.

In spite of the fact that these 5 profiles were done with the identical sample, the profiles exhibit distinctive differences, originating from the different alignment procedures.

When performing "neither an adjustment of the sample thickness, nor an axis alignment" (=**Red**),

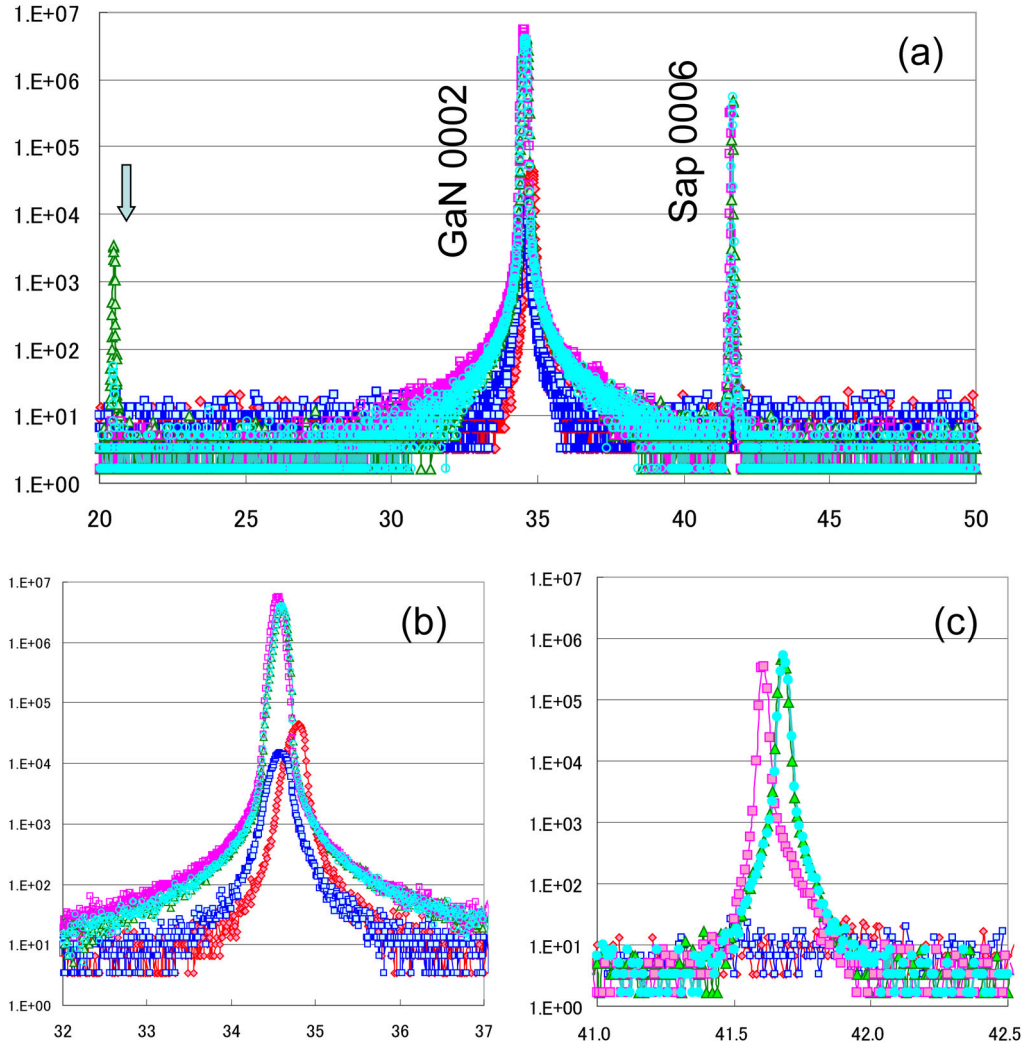

Fig. 4. (a) $2\theta/\omega$ profiles for GaN on Sap, (b) A close-up view around GaN 0002 reflections, (c) A close-up view around Sap 0006 reflections.
Horizontal axes were 2θ angles with CuKα_1, and vertical axes were shown in a.u. of log scales.

or only with a thickness adjustment of a sample (=**Blue**), the appropriate data were not obtained, in the sense that the peaks of Sap were not detected, or the peaks of GaN reflections were shifted in positions or weak in intensity. It is interesting to note that there exist marked differences between the Sax Blue profile with the axis alignment for Sap 0006 reflection, and the Pink profile with the axis alignment for GaN 0002 reflection. This is the influence of a miscut substrate (or often called an off-cut substrate). In a miscut substrate, the macroscopic surface of the single crystalline substrate was intentionally treated as not parallel with the lattice plane of substrate crystals in the cutting/polishing processes. Miscut substrates are often employed for the growth of epitaxial film with large lattice mismatch between substrates. The term "vicinal substrate" is used for a substrate with a small miscut angle (the intersecting angle between the macroscopic surface and the lattice plane).

As a result of employment of miscut substrates, epitaxial thin films on these substrates sometimes exhibit a misorientation of its lattice against the substrate lattice[14),(15)]. In the present sample, it was confirmed that there existed a slight misorientation (0.04°) between the *c*-axis of GaN and the *c*-axis of Sap. This slight misorientation is the origin of the differences between the Sax Blue profile and the Pink profile. The difference was clearly observed in Fig. 4(c), since the Sap 0006 reflection is so sensitive to a slight error in the ω-axis alignment due to the extremely narrow rocking curve width. The misorientation in Sap(0001) substrates is generally introduced since the plane formed by the *c*-axis of the Sap lattice and the axis of the surface normal is parallel with the orientation flat in the substrate outer edge. Therefore it is recommended to check the existence of this misorientation between the *c*-axis of GaN and the *c*-axis of Sap when the GaN/Sap sample was set on the XRD diffractometer such as the orientation flat of the Sap substrate laid parallel to the direction of the incident X-rays.

In cases of other kinds of substrates (for instance, *a*-Sap (=(11$\bar{2}$0)), *r*-Sap (=(01$\bar{1}\bar{2}$)), or *m*-SiC (1$\bar{1}$00)), or of substrates with a large miscut, the anisotropy within the interface planes between the epitaxial GaN films

and the substrates will be introduced. This anisotropy influences the crystallinity of GaN films and their lattice distortion/lattice relaxation. Therefore, it is recommended to measure ω-scan rocking curves for GaN films (a characterization of tilting mosaicity) at both ϕ=0° and ϕ=90° after the axis alignment for the diffraction peak of substrates. This allows you to check the misorientation between films and substrates, and to check the anisotropy of mosaic spread of epitaxial films.

Caution is required in the process of refinement of lattice constants from the $2\theta/\omega$ profiles for samples with misorientation between films and substrates. It is desirable to run two $2\theta/\omega$ scans after the axis alignment procedure for the diffraction peak of substrates and for the diffraction peak of films, respectively.

In the SmartLab^{TM} system, a useful device, "Rx–Ry attachment head",[16] is available. This device is composed of two orthogonal tilt-adjusting swivels, and is mounted on the ϕ-rotation stage. This allows the axis of lattices to be aligned to the ϕ-rotation axis of the goniometer. By utilizing this attachment head, the angle of the misorientation and the azimuthal direction of this misorientation can be easily analyzed. This function of the "Rx–Ry attachment head" is also helpful for the analysis of lattice distortion in epitaxial films through the data analysis of Reciprocal Space Map (RSM) measurements for the asymmetrical lattice planes (see section 3.4).

A sharp peak around 2θ=20° (marked with the arrow) was found only for the Green profile in Fig. 4(a). Judging from its 2θ angle, this peak can be indexed as the 0003 reflection of Sap, but this reflection is a so-called "forbidden reflection", whose intensity should be 0.

The diffraction signal for this peak originates from the phenomena of multiple Bragg diffractions[17]–[21].

Some of readers may have an experience to detect a sharp peak around 2θ=32.9° in the measurement of $2\theta/\omega$ scans for Si(001) substrates. This peak could be indexed as the Si 002 reflection, which is a "forbidden reflection", but it was observed by the effect of multiple reflections.

The multiple Bragg diffractions are caused by the contributions of the multiple scattering of lattice planes including asymmetric lattice planes (inclined lattice plane against the surface plane). This fact implies that the occurrence of this phenomenon should be sensitively dependent on the azimuthal position (ϕ-axis angle).

Two $2\theta/\omega$ scan profiles of a GaN/Sap sample were shown in Fig. 5. The profile in blue is the one where the orientation of the Sap substrate was carefully aligned so that the $[1\bar{1}00]$ axis lies parallel to the incident X-rays and then the c-axis was aligned to the ϕ rotation axis. On the other hand, the profile in purple was acquired after the sample was rotated with ϕ-axis by 9°. In the figure, the peaks due to the multiple Bragg reflections were shown with framed labels of their reflection indices. The multiple reflections were found not only for Sap 0003 reflections, but also for Sap 0009 and

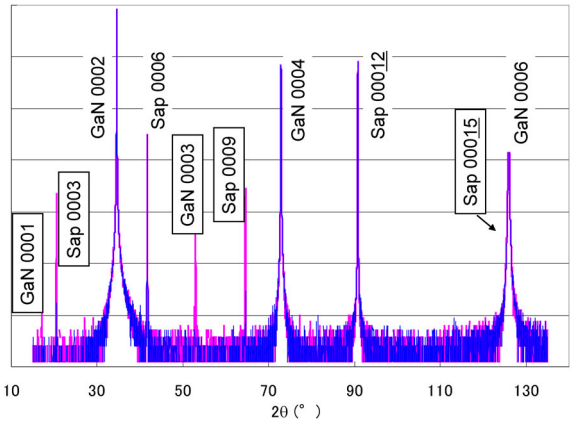

Fig. 5. A wide range $2\theta/\omega$ profiles for GaN/Sap sample.

00015 reflection in the profile in purple. In addition, the multiple reflections for GaN (0001 and 0003 reflections) were also detected. In the profile in blue, peaks caused by the multiple reflections could not be clearly detected, except for the Sap 0003 reflection. This result reveals that the occurrence of the multiple Bragg diffractions is dependent on the ϕ rotation angle. And, you can see that we can greatly suppress the effect of multiple reflections when the c-GaN/c-Sap sample is set in the configuration where the orientation flat of the Sap substrate is lying parallel to the incident X-rays.

3.2. Evaluation of the twisting mosaicity

As was discussed in the preceding article, GaN epitaxial growth on a Sap substrate is a heteroepitaxial system with large lattice mismatch. For this system, the characterization of its crystalline quality should be performed not only along the growth direction (tilting mosaicity), but also for the azimuthal orientation distribution of crystallites (domain) within the interfacial plane (twisting mosaicity) [16],[22]–[28].

The SmartLab^{TM} system for thin films equipped with the "In plane" measurement axis has two alternative geometries for a sample configuration to access to the corresponding lattice planes.

1) by tilting a sample with χ-axis by 90°
2) by utilizing the in plane measurement axis while a sample is set on the horizontal plane

The former geometry is possible with conventional four-circle goniometer systems dedicated for thin film samples. But, mainly due to the insufficient surface-sensitivity, diffraction signals obtained were generally weak. In contrast, a significant surface-sensitivity is realized with the combination of designs of incident X-ray optics and the employment of the in plane measurement axis in the latter geometry.

These two geometries are available in the SmartLab system for thin films and it provides a freedom of choice between the two configurations depending on the requirement about the surface–sensitivity or the resolution of measurements [16],[27].

Since the diffraction signals are generally weak, the

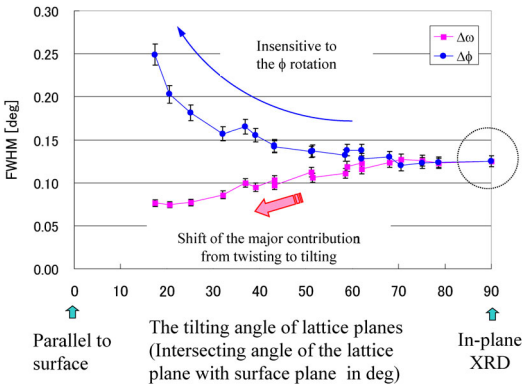

Fig. 6. Rocking curve widths of various lattice planes.

characterizations by the rocking curve measurements for the asymmetric lattice planes with a skew geometry (tilting with χ-axis) have been supplementalily employed for the evaluation of twisting mosaicity in GaN-related materials.

In the case of *c*-axis grown GaN epitaxial films, the asymmetric lattice planes, such as $(10\bar{1}3)$, $(10\bar{1}2)$, $(10\bar{1}1)$, $(20\bar{2}1)$, have been employed as reported in the literature for the evaluation of twisting mosaicity. The inclination angles for these lattice planes against the *c*-plane (*i.e.*, (0001)) are 32°, 43°, 61°, 75°, respectively.

Figure 6 shows plots of rocking curve widths (FWHM values) of various reflections of epitaxial *c*-GaN on *c*-Sap as a function of the tilting angles of the χ-axis. Twisting mosaicity was evaluated as 0.125° from the "in plane" XRD rocking curve width for the $10\bar{1}0$ and $11\bar{2}0$ reflections using the in plane measurement axis. In the figure, rocking curve widths of ω-scans (colored with purple) and ϕ-scans (colored with blue) were plotted.

The right side end (tilting of 90°) of the figure corresponds to the geometry of in plane XRD measurements, where the rocking curve widths of ω-scans and ϕ-scans showed the same value of 0.125°. This result is reasonable because the rotating axes for ω-scans and ϕ-scans coincide with each other in the configuration of this geometry. Note that these values are in good agreement with the one obtained in the measurement using the "in plane" measurement axis.

The rocking curve widths of ω-scans become narrower with the decrease of the tilting angles. This tendency can be explained from the fact that the major contribution for the peak breadth shifts from the twisting mosaicity to tilting mosaicity with the decrease of the tilting angles[23)–25)]. On the other hand, the value of the rocking curve widths for ϕ-scans became larger with the decrease of the tilting angles. This situation can be described as followed. The axis of ϕ-rotation tends to deviate from the axis of ω-rotation with the decrease of the tilting angle, approaching the configuration where these two axes intersect with each other by 90° at the tilting angle of 0°(the left hand end of the Fig. 6). In the final configuration, the diffraction condition will not show any sensitivity with the variation of ϕ angle, thus the rocking curve width should diverge.

Roughly speaking, we can regard the rocking curve widths of ω-scans for the lattice planes with the tilting angles over than 60° as the approximated values for the twisting mosaicity. However it is better to perform some data corrections for the data of lattice planes with the tilting angle below 60° for the precise analysis of twisting[24),25)].

3.3. Effect of the sample curvature and the procedure to evaluate the curvature

Large lattice mismatch is one of the greatest obstacles to growing high quality GaN epitaxial films on Sap or other foreign substrates. Another obstacle is the large mismatch in the thermal behaviors, especially the mismatch in the thermal expansion coefficients, because the epitaxial growth from vapor phases is generally performed under extremely high temperature (around 1000℃), being followed by the cooling process to ambient conditions. This great departure in processing temperatures, together with a large mismatch in thermal expansion coefficients, will be another cause promoting the elastic distortion of lattices of epitaxial layers leading to the curvature of the sample.

The linear thermal expansion coefficient for the *a*-axis of GaN is smaller than that of Sap but is larger than the corresponding coefficient of Si. So, the compressive stress within the surface plane will be applied to GaN epitaxial films on Sap after recovering from the growth conditions to room temperature. On the contrary, GaN on a Si substrate will suffer with tensile stress after recovery. For this reason, in the case of the GaN epitaxial thin film on Sap substrates, samples exhibit a convex curvature on the GaN film side, whereas samples of GaN on a Si substrate exhibit a concave curvature on the GaN film side.

This section explains how the curvature affects the XRD data and describes the procedures to characterize the curvature of samples by XRD techniques.

Let us see the influence of sample curvature on XRD data, first.

Orientation dispersions or fluctuations are inherent in a single crystalline sample with curvature. (Fig. 7) Therefore the rocking curve width should be broadened[29)], as the summation of the intrinsic peak breadth, optical resolution, and the broadening due to curvature. As a consequence, peak broadening in the profiles of $2\theta/\omega$ scans also occur.

In order to avoid this situation, the restriction of the area of X-ray exposure by using a narrow slit in the incident side of X-ray optics is helpful.

$2\theta/\omega$ scan profiles around 0002 reflections of a sample with a InGaN/GaN multi quantum well (MQW) superlattice structure on a *c*-Sap substrate are shown in Fig. 8. These profiles were measured with slit sets of 1.0 mm width (purple line) and of 0.1 mm width (blue line) for both the incident slit and the receiving slit. Although, satellite peaks originating from the MQW superlattice[1)–4),26)] could be clearly observed in both profiles, fringes of fine pitches caused by the total

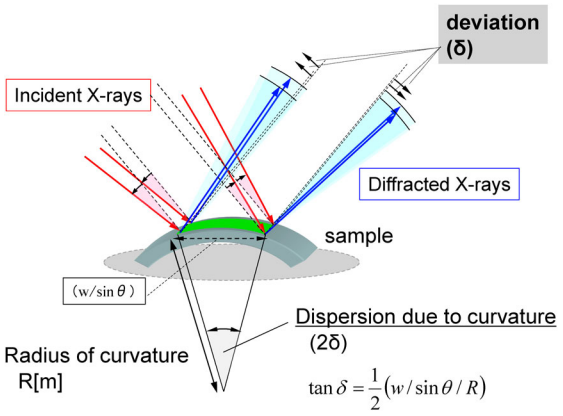

Fig. 7. A schematic illustration for the cause of broadening of rocking curve width for a sample with curvature.

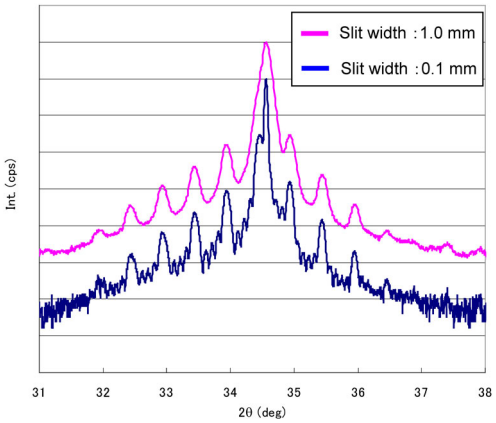

Fig. 8. $2\theta/\omega$ scan profiles of InGaN/GaN-MQW layer structure with the slits of different width.

amount of thickness could be detected only in the profile with the slit set of 0.1 mm width (blue line). The peak separation of the 0th order satellite peak (shown with black arrows in Fig. 8) and the 0002 reflection from the GaN buffer layer was not clear in the profile with the slit set of 1.0 mm width (purple line). The radius of curvature in this sample was preliminarily evaluated as 7 m by the XRD method, mentioned later.

Another approach to suppress the influence of the sample curvature is the employment of the analyzer crystal device in the receiving optics side. This optics configuration equipped with the analyzer crystal device and with the incident monochromator collimator devices (beam conditioners) is called the "triple-crystal" configuration. The optics configuration with only the incident monochromator collimator devices in the HR-XRD measurement for single crystalline samples is called the "double-crystal" configuration.

The resolution of the optics with the analyzer crystal is defined by the intrinsic rocking curve width of the diffraction of the analyzer crystal employed. It generally ranges from 0.001 to 0.005°. The resolution of the optics with the double receiving slits configuration is variable using the capture angles of the collimation by double receiving slits. It ranges approximately from 0.01 to 0.1°, depending the slit widths. The employment of sets of the double receiving slits together with the narrow incident slit may be covenient in some cases, due to the flexibility of balancing the resolution required and the signal intensity obtained.

A method for evaluating the curvature in a sample (lattice plane) by XRD is explained in this section. If rocking curve measurements are carried out for a sample without curvature, positions of peak tops in the rocking curve profiles will not show any shifts, when a sample is moved using an X−Y sample mapping stage attachment to change the position of analysis on the sample surface. However, a sample with curvature (inherent with the curvature of lattice plane) will exhibit a shift of peak top positions in the same measurement procedures (Fig. 7). This peak shift can be analyzed by plotting this shift with a function of translation (travelling length)

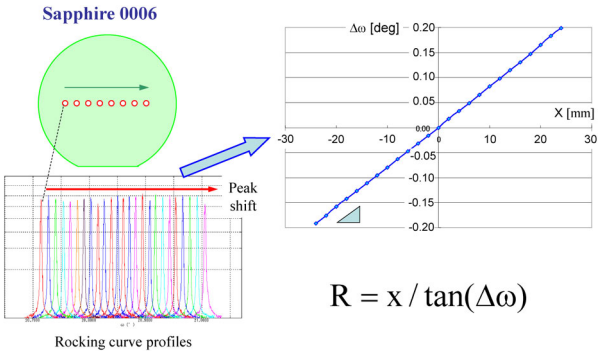

Fig. 9. An example of Curvature analysis of a Sap substrate by XRD.

of a sample. An example of the curvature analysis for a Sap substrate with an InGaN/GaN MQW superlattice structure (the same sample that was used to create Fig. 8) is shown in Fig. 9. Rocking curves were measured for the 0006 reflection of Sap. The radius of curvature was calculated as 7 m by the simple equation shown in Fig. 9. The linear slope of plots shown in the graph at the right side of the figure indicates that the curvature in this sample is uniform all over the sample surface.

This method can also be applied to a bare single crystal wafer. Please note that this method can evaluate the curvature of lattice planes (*i.e.*, the waving of lattices). There might be a discrepancy from the result of the curvature analysis by this method, and the result by surface topographic analyses, such as a laser interferometry, etc, since a surface plane does not necessarily run parallel to the lattice plane of the wafer as a whole.

In order to perform a precise analysis of curvature in a sample of with a large radius of curvature (this means that the curvature of the sample is extremely small), the uncertainty errors caused from factors other than from the sample curvature should be suppressed. Other two influencing factors are 1) the ambiguity in determining the peak top positions, and 2) the mechanical fluctuation of the sample during the X−Y movements. The former factor can be suppressed by using the incident optics and by using the narrow slit sets to limit the area of analysis

on the sample surface. The latter factor can be cancelled in the data analysis by referring to the data with flat wafers. A thick wafer might be replaced for flat wafers, for this purpose.

3.4. Analyses of RSM data

The information concerning the compositions in solid solution systems, such as AlN-GaN, InN-GaN, is very important for device fabrication and control of their performances. In order to evaluate the composition variations in the solid solution epitaxial thin films, it is required to know the influences of the lattice distortions caused by the constraints to the substrates. The analyses of the RSM data for a asymmetric lattice planes are performed due to this requirement[(1)–(4),(26)].

From the analyses of the RSM data for an asymmetric lattice plane, interplanar distances of lattice planes both along the growth direction and along the interface (surface) planes can be obtained independently[(30),(31)]. Please see the references, (1)–(4), (15), (26) for more details to understand the basics and the theoretical background of the RSM measurements and analyses.

The key point in the RSM data analysis is how to convert the XRD data which are with the goniometer coordinates, (ω, 2θ) to 2D data in reciprocal space coordinates, through the interpretation of the orientation relationships between the reciprocal space coordinates and the crystallographic lattices of samples. The q_z axis of the reciprocal coordinates corresponds to the goniometer coordinates where the ω value coincides with the half value of 2θ. The alignment between the reciprocal space coordinates and the crystallographic lattice(s) through their translations to the goniometer coordinates is done by the process to define the relative position of ω to 2θ. If you set the ω value to the half of 2θ value after the axis alignment (see section 3.1) of the crystallographic lattice plane of interest, this alignment of coordinates and the crystallographic lattice is completed for the q_z axis. The lattice planes close to parallel to the surface planes (hence, the growth plane) are generally employed.

In this axis alignment process, the alignment of a crystallographic axis to the ϕ-rotation axis utilizing the "Rx−Ry attachment head" device (see section 3.1) and the "precise alignment" procedure in the "SmartLab Guidance" controlling software, will greatly make the peak search of asymmetric lattice planes easier, or make the RSM data analysis simpler. This is because, it is guaranteed that the q_z axis was already aligned to the crystallographic lattice of interest and the goniometer coordinates at any positions of the ϕ-axis.

Two RSM data around GaN $11\bar{2}4$ reflections of *c*-GaN on *c*-Sap (the same sample shown in Figs. 4 and 5) are shown in Fig. 10. These two data were measured after the different axis alignment process for the axis along the film growth direction. Figure 10(a) is the RSM data after the axis alignment for the GaN 0002 reflection (this data was taken after the measurement of the $2\theta/\omega$ scan shown in Pink in the Fig. 4(a) to (c)) at section 3.1. While, Fig. 10(b) is the RSM data after the axis alignment for the Sap 0006 reflection (this data was taken after the measurement of the $2\theta/\omega$ scan shown in Sax Blue in the Fig. 4(a) to (c)). The result of calculations for the lattice constants, deduced each RSM data is shown in the figure. Since these data were measured for the same sample, it is clear that these differences in the deduced lattice constants was caused from the difference in the axis alignment procedure. As is discussed in section 3.1, it was confirmed that there exists a misorientation between the GaN film and the Sap substrate in this sample. This implies that the crystallographic lattices for GaN and Sap should be correlated with each other by the rotation angle of 0.04°. For the analysis of lattice constants in GaN epitaxial film of this sample, the result shown in Fig. 10(a) is correct. The rotation for the RMS data in Fig. 10(b) around the origin of the reciprocal space by 0.04° in the counter-clockwise direction can also lead to the correct result.

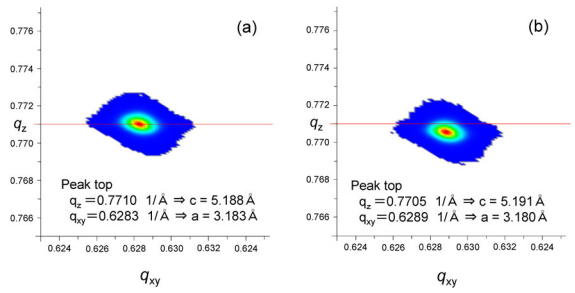

Fig. 10. RSM data around GaN $11\bar{2}4$ reflections measured after different axis alignment procedures (reciprocal coordinates are shown in 1/d = 1/Å).

It may be reasonable to assume that the misorientation angle in the present example may be relatively small, if it is noticed that the miscut angles are designed in the range of 0.1 to 0.5° for the commercially available Sap substrates for the epitaxial growth of GaN films.

Next, the lattice distortion due to the constraint to substrates in epitaxial GaN films grown along its *c*-axis is discussed.

The strain along the *c*-axis (ε_{zz}) is expressed as $\varepsilon_{zz}=c_{obs}/c_0-1$, and the strains within the interface plane (thus, can be represented as along *a*-axis under the assumption of the isotropic stress field within the interface plane) (ε_{xx}) can be expressed as $\varepsilon_{xx}=a_{obs}/a_0-1$, where a_0 and c_0 are the values of lattice constants without stress along the *a*-axis and *c*-axis, respectively, and a_{obs} and c_{obs} are the observed values of lattice constants along the *a*-axis and *c*-axis, respectively. The elastic deformation theory denotes the relationship between ε_{xx} and ε_{zz} in the formula as below[(1),(3)–(5),(30),(31)],

$$\varepsilon_{zz}=\frac{2C_{13}}{-C_{33}}\varepsilon_{xx} \quad (1)$$

where C_{ij} is the elastic stiffness coefficients of GaN single crystals.

In most cases for epitaxial GaN films on Sap or Si,

thick buffer layers are introduced to accommodate the large lattice mismatches between GaN films and substrates. So, the MQW layers are mostly expected to be relaxed by relieving their lattice strains caused from the large lattice mismatching via constraining to substrates. Instead, the lattice distortion caused by the mismatch of the thermal expansion nature between films and substrates should be taken into accounts. (see the preceding article of this series)

If we can assume that the residual strains in GaN epitaxial thin films are mainly caused by the thermal stress originating from the mismatches between films and substrates, it is possible to make a rough estimation of the growth temperature of GaN films.

For example, let us see the case where a single layer of GaN grew epitaxially on a Si (111) substrate at the growth temperature of T_g, and it was cooled down to room temperature.

Under the assumption where the strains in the GaN film caused by the lattice mismatch was totally relieved, the lattice constant of the *a*-axis of GaN within the interface plane after the recovery to room temperature is expressed as followed.

$$a_{Tg} = a_0 + a_0 \times \alpha_{GaN,a} (T_g - T_{RT}) \quad (2)$$

where a_0 is the values of lattice constants without stress along the *a*-axis, and $\alpha_{GaN,a}$ is the coefficient of linear thermal expansion along *a*-axis of GaN. Since it was cooled from the growth condition at T_g to room temperature as was constrained to the Si substrate, the resultant lattice constant of *a*-axis at room temperature (a_{RT}) can be denoted by the following formula.

$$a_{RT} = a_{Tg} - a_0 \times \alpha_{Si} (T_g - T_{RT}) \quad (3)$$

Where, α_{Si} is the coefficient of linear thermal expansion along the *a*-axis of Si. Since a Si crystal has an isometric (cubic) symmetry, the coefficient of linear thermal expansion along *a*-axis can represent that along the $[1\bar{1}0]$ or $[11\bar{2}]$ axis of Si within the interface plane.

By combining equations (2) and (3), the following formula is obtained.

$$T_g = T_{RT} + (a_{RT} - a_0)/a_0 (\alpha_{GaN,a} - \alpha_{Si}) \quad (4)$$

Note that the coefficients of linear thermal expansion were assumed to be constant and their temperature dependency was ignored in this discussion.

4. Current hot technical topics

4.1. Non-polar or semi-polar growth

Since the growth direction (*c*-axis) coincides with the polar direction of GaN epitaxial films on Sap (0001) or Si(111), the electric device performance is affected by the intrinsic spontaneous and/or piezoelectric polarization field. In recent years, the approaches to grow GaN epitaxial thin films along semi-polar or non-polar directions have been widely studied[32]–[34].

In the cases of semi-polar or non-polar GaN single crystal growth, the symmetry around the growth axis of GaN films should be treated as anisotropic. Furthermore, semi-polar or non-polar GaN growth is performed on non-isotropic lattice planes (not isotropic around the axes perpendicular to the lattice planes) on substrates, such as *m*-plane or *a*-plane of ZnO substrates, *r*-plane Sap, Si (113), *m*-plane SiC, GaAs (110), *a*-plane γ-$LiAlO_2$ etc.

Therefore, as was explained in section 3.1, great attentions should be paid for the analyses of the mis-orientations between films and substrates or the anisotropic lattice deformations in the characterization of crystallinity of semi-polar non-polar GaN epitaxial films.

Some studies on non-polar GaN-related materials or ZnO films are now introduced.

Kawai[35] reported an epitaxial growth of (In,Ga)N solid solution thin films grown by the MOVPE method on the ZnO single crystal substrates of various lattice planes (*a*-planes, *m*-planes, and *c*-planes).

The variations of the crystalline quality of (In,Ga)N epitaxial thin films and In (indium) incorporation to films were discussed as functions of growth directions and the differences in growth temperature by using the high-resolution XRD technique and the PL (photoluminescence) characterization technique. For the films grown on *a*-planes and *m*-planes of ZnO substrates, the crystalline (tilt) anisotropy and the anisotropy of lattice distortion were discussed from the analysis of the result of two or more RSM data.

Murakami *et al.*[36] reported a semi-polar InN growth on a nonpolar (110) GaAs substrate grown by MOVPE method. It was found from the XRD $2\theta/\omega$ scans that the growth plane of InN was quasi-parallel to the GaAs(110). The *c*-axis of InN was revealed from the analysis of XRD pole figure measurement data to preferentially align with one of the two [111] axes (either [111]A or [111]B) of GaAs, which was inclined by 35° from the surface normal. Finally, the InN film was confirmed to grow with the epitaxial orientation relation as InN(0001)//GaAs(111)B, with the result of the polarity determination using XRD technique (see section 4.2).

Han *et al.*[37] and Zhylik *et al.* [38] reported *a*-plane growth of ZnO films on *r*-plane Sap substrates grown by the plasma-assisted MBE (PAMBE) method.

A clear anisotropy in tilt spread values for the *a*-axis (growth axis) of ZnO films could not be observed from the rocking curve analysis by changing the azimuthal directions. However, the lattice of ZnO epitaxial films showed a remarkable anisotropic distortion within surface planes. It was confirmed from the in plane XRD measurements that the *m*-axis of ZnO was expanded by the tensile stress, while *c*-axis of ZnO was shrunk by the compressive stress. It was also revealed that the peak shift of PL was in good concordance with the strain values of the *c*-axis of ZnO.

4.2. Crystallographic polarity determination by XRD

The determination of a polar direction has been performed by various techniques[8], such as, the chemical etching techniques, electron diffraction techniques (RHEED: reflective high-energy electron diffraction method or CBED: convergent-beam-electron-diffraction method etc.), or a CoAxial Impact Collision Ion Scattering Spectroscopy (CAICISS) method, etc.

In 1928, Nishikawa and Matsukawa[39] suggested the possibility of the crystallographic polarity determination by XRD in a non-destructive way though the comparison of the diffraction intensity utilizing the anomalous X-ray scattering phenomena at the X-ray wavelength around the absorption edge of constituent atoms. Mariano and Hannemann[40] succeeded in determining the crystallographic polarity of ZnO single crystals using a laboratory XRD apparatus.

The success in determining the crystallographic polarity in noncentrosymmetric single crystals using XRD is to employ X-rays whose wavelength is close to the absorption edge of constituent atoms. The principles in this determination method are briefly described.

The term of "Structure Factor" was explained in common textbooks for XRD as,

$$F_{hkl}=\sum_{j}(f_{0,j}+\boxed{\Delta f_j'+i\Delta f_j''})\exp(2\pi i(hx_j+ky_j+lz_j)) \quad (5)$$

Where, is the structure factor of *hkl* reflection, $f_{0,j}$ is the atomic scattering factor of *j*th atom in the unit cell, and $\Delta f_j'$ and $\Delta f_j''$ are the anomalous scattering terms for the *j*th atom in the unit cell. (x_j, y_j, z_j) is the fractional coordinates of *j*th atom in the unit cell. Since, these anomalous scattering terms (marked with a red frame in equation (5)) are smaller than the $f_{0,j}$ term, they are treated as negligible in the conventional XRD measurements. Consequently, $|F_{hkl}|$ equals to $|F_{\bar{h}\bar{k}\bar{l}}|$, and the crystallographic polarity direction cannot be determined. However, when XRD measurements are made with an X-ray wavelength around the absorption edge, these anomalous scattering terms cannot be neglected. In this condition, the structure factor, F_{hkl}, should be treated as proportional to $\sqrt{F_{hkl}\times F_{hkl}^{*}}$. As a result, $|F_{hkl}|$ does not equal to $|F_{\bar{h}\bar{k}\bar{l}}|$, and then, the difference in the diffraction intensities for these lattice planes can be applied for the determination of the crystallographic polarity.

The X-ray wavelength of the K absorption edge of a Ga atom is 0.11957 nm. This wavelength is far from the wavelength of the characteristic line of Cu Kα_1, (λ=0.154059 nm). So, the polarity determination of GaN is almost impossible by using Cu Kα_1 radiation.

Then, another approach was tried for the determination of GaN polarity. In the reference (41), a Au (gold) rotating anode was employed as an X-ray source, and the Au L-radiation was collimated and monochromated by the use of an X-ray multilayer mirror as an incident optic device.

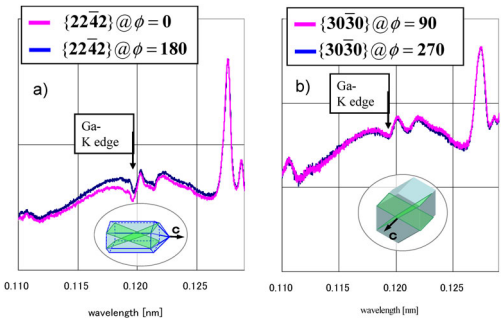

Fig. 11. XRD profiles of a-GaN on r-Sap(a) for semi-polar 22$\bar{4}$2 reflections, and (b) for non-polar 30$\bar{3}$0 reflections. Vertical axis is the intensity of a.u., in log scales.

The sample was the 2 μm-thick GaN epitaxial thin film grown along the non-polar *a*-axis by the MOVPE method on *r*-plane Sap. The polar *c*-axis of GaN lay in the surface plane.

The polarity determination was performed by comparing the diffraction intensities of reflections for semi-polar lattice planes, 22$\bar{4}$2 and 22$\bar{4}\bar{2}$, which were tilted by 31.6° from the surface plane, and could be accessed to each other simply by the 180° rotation of around the surface normal axis. Profiles measured were shown in Fig. 11(a). The measurement shown here was performed by simple $2\theta/\omega$ scans. In this figure, the horizontal axis is shown with the value of the wavelength. The conversion from the 2θ angle to the wavelength was performed by using the Bragg equation, λ=2d sinθ, since the d value for these lattice planes are known.

In Fig. 11(a), the difference of the diffracted intensity can be clearly observed in the region of the X-ray wavelength below the Ga K absorption edge (λ= 0.11957 nm). Since $|F_{22\bar{4}2}|$ was known to be smaller than $|F_{22\bar{4}\bar{2}}|$ from the theoretical calculation, it is possible to distinguish the semi-polar 22$\bar{4}$2 and 22$\bar{4}\bar{2}$ reflections. For a comparison, diffraction profiles of non-polar 30$\bar{3}$0 reflections for the asymmetric lattice planes tilted by 30° from the surface plane are shown in Fig. 11(b). Since these are the non-polar lattice planes, no differences can be found in two profiles shown in of Fig. 11(b).

Since this technique is applicable to a material system containing Ga atom, it is applicable not only to pure GaN but also to solid solution systems, such as (In,Ga) N and (Al, Ga)N. Moreover, it is applicable also to material systems, such as GaAs, GaP, or GaSb with ZB type crystal structure.

Furthermore, since the X-ray wavelength of the Zn (zinc) K absorption edge (λ=0.12833 nm) is also close to the K absorption edge wavelength of Ga atom, the optic system with Au L-radiation X-rays can be adopted for the polarity determination for ZnO or ZnS, etc.

5. Summary

A HR-XRD technique has been widely applied for the characterization of the heteroepitaxial compound

semiconductor epitaxial films. As a consequence, a great advancement has been promoted in XRD measurement technology, its analysis methodology, and measurement components.

In the present special feature articles, technical notifications and hot issues for the application of HR-XRD in the characterization of GaN related materials for opto-electronic and power-electronic applications were explained. Heteroepitaxial growth of GaN-related materials can be contrasted with that of GaAs-related materials, due to the difference in their crystallographic natures, or the mismatches to the substrate materials. These articles were designed to emphasize the technical notifications by comparing with the application of XRD techniques to GaAs-related materials.

Furthermore, GaN-related materials are now in stages of active researches where, bulk single crystal growth are demonstrated, device fabrication with semi-polarity and non-polar epitaxial film are studied, etc. toward the development for the new functional and highly efficient electronic devices of the future. HR-XRD techniques are to be employed as powerful and indispensable tools in this field, and also hopefully for the possible functional materials in future.

Rigaku is pleased if these articles can serve as technical references in guiding readers to fruitful results.

References

(1) D. K. Bowen and B. K. Tanner: *"High Resolution X-ray Diffraction and Topography"* Taylor & Francis Inc. (1998).
(2) U. Pietsch, V. Holy and T. Baumbach: *"High-resolution X-ray Scattering—From Thin Films to Lateral nanostructures"* Springer-Verlag, (1999).
(3) P. F. Fewster: *"X-ray scattering from Semiconductors"*: Imperial College Press, (2000).
(4) M. Birkholz: *"Thin film Analysis by X-ray Scattering"* Wiley-VCH Verlag GmbH & Co., (2006).
(5) O. Ambacher: *J. Phys. D: Appl. Phys.*, **31** (1998), 2653−2710.
(6) K. Balakrishnan, G. Feuillet, K. Ohta, H. Hamaguchi, H. Okumura and S. Yoshida: *Jpn. Jour. Appl. Phys.*, **36** (1997), 6221−6225.
(7) C. H. Bates, W. B. White and R. Roy: *Science*, **137** (1962), 993.
(8) E. S. Hellman: *MRS Internet Journal of Nitride Semiconductor Research*, **3** (1999), Article 11.
(9) F. Bernardini, V. Fiorentini and D. Vanderbilt: *Phys. Rev.*, **B56** (2009), R10 024−027.
(10) E. H. Kisi and M. M. Elcombe: *Acta Cryst.*, **C45** (1989), 1867.
(11) J. E. Jaffe and A. C. Hess: *Phys. Rev.*, **B48** (1993), 7903.
(12) L. Gerward and J. S. Olsen: *J. Synchrotron Radiat.*, **2** (1995), 233.
(13) T. Minegishi, J. H. Yoo, H. Suzuki, Z. Vashaei, K. Inaba, K. Shim and T. Yao: *Jour. Vac. Sci. and Technol.*, **B23** (2005), 1286−1288.
(14) H. K. Chauveau, P. De Mierry, H. Cabane and D. Gindhart: *Jour. Appl. Phys.*, **104** (2008), 113516-1−113516-7.
(15) T. Yuasa, Y. Ueta, Y. Tsuda, A. Ogawa, M. M. Taneya and K. Takano: *Jpn. Jour. Appl. Phys.*, **38** (1999), L703−L705.
(16) S. Kobayashi: *Rigaku Journal (English version)*, **26** (2010), No. 1. 3−11.
(17) Von M. Renninger: *Acta Cryst.*, **8** (1955), 606−610.
(18) C. A. B. Salles da Costa, L. P. Cardoso, V. L. Mazzocchi and B. R. Parente: *Jour. Appl. Cryst.*, **25** (1992), 366−371.
(19) J. Bläsing and A. Krost: *Phys. Stat. Sol. -A*, **201** (2004), R-17−R20.
(20) J. Z. Tischeler, J. D. Budai, G. E. Ice and A. Habenschuss: *Acta Cryst.*, **A44** (1988), 22−25.
(21) S. A. Stepanov and A. P. Ulyanenkov: *Acta Cryst.*, **A50** (1994), 576−585.
(22) O. Ambacher: *J. Phys. D: Appl. Phys.*, **31** (1998), 2653−2710.
(23) H. Heinke, V. Kirchner, S. Einfeldt and D. Hommel: *Appl. Phys. Lett.*, **77** (2000), 2145−2147.
(24) S. R. Lee, A. M. West, A. A. Allerman, K. E. Waldrip, D. M. Follstaedt, P. P. Provencio, D. D. Koleske and C. R. Abernathy. *Appl. Phys. Lett.*, **86** (2005), 241904-1−241904-3.
(25) H. Li, Y. Luo, L. Wang, G. Xi, Y. Jiang, W. Zhao and Y. Han: *Appl. Phys. Express*, **1** (2008), 045004-1−045004-3.
(26) T. Konya: *Rigaku Journal (English version)*, **25** (2009), No. 2. 1−8.
(27) S. Kobayashi and K. Inaba: *Rigaku Journal*, **28** (2012), No. 1. 8−13.
(28) Y. J. Sun, O. Brandt, T. Y. Liu, A. Trampert, K. H. Ploog, J. Bläsing and A. Krost: *Appl. Phys. Lett.*, **81** (2002), 4928−4930.
(29) T. Paskova, L. Becker, T. Böttcher, D. Hommel, P. P. Paskov and B. Monemar: *Jour. Appl. Phys.*, **102** (2007), 123507-1−123507-4.
(30) S. Pereira, M. R. Correia and E. Pereira, K. P. O'Donnell, E. Alves, A. D. Sequeira, N. Franco, I. M. Watson and C. J. Deatcher: *Appl. Phys. Lett.*, **80** (2002), 3913−3915.
(31) M. A. Moram and M. E. Vickers: *Rep. Prog. Phys.*, **72** (2009), 036502-1−036502-40.
(32) F. Oehler, M. E. Vickers, M. J. Kappers and R. A. Oliver: *Jour. Appl. Phys.*, **114** (2013), 053520-1−053520-12.
(33) M. Frentrup, N. Hatui, T. Wernicke, J. Stellmach, A. Bhattacharya and M. Kneissl: *Jour. Appl. Phys.*, **114** (2013), 213509-1−213509-10.
(34) H. Jönen, H. Bremers, U. Rossow, T. Langer, A. Kruse, L. Hoffman, J. Thalmair, J. Zweek, S. Schwaiger, F. Schplz and A. Hangleiter; *Semicond. Sci. Technol.*, **27** (2012), 024013-1−024013-8.
(35) Y. Kawai: "Study on GaInN growth on ZnO substrates by Metalorganic Vaper Phase Epitaxy", Doctoral Thesis, Meijyo University, Japan (2009).
(36) H. Murakami, H. C. Cho, M. Suematsu, K. Inaba, Y. Kumagai and A. Koukitu; *Phys. Stat. Sol. -C*, **9** (2012), 677−680.
(37) S. K. Han, D. C. Oh, J. H. Song, K. Inaba, T. Yao and S. K. Hong: *Appl. Phys. Express*, **5** (2012), 081101-1−081101-3.
(38) A. Zhylik, A. Benediktovitch, I. Feranchuk, K. Inaba, A. Mikhalycheva and A. Ulyanenkov: *Jour. Appl. Cryst.*, **46** (2013), 919−925.
(39) S. Nishikawa and K. Matsukawa: *Proc. Imp. Acad. Japan*, **4** (1928), 96.
(40) A. N. Mariano and R. E. Hanneman: *Jour. Appl. Phys.*, **34** (1963), 384.
(41) K. Inaba and H. Amano: *Phys. Stat. Sol. -B*, **244** (2007), 1775−1779.